The Astrophysical Journal, 693:1128–1132, 2009 March 10 doi:10.1088/0004-637X/693/2/1128

PULSED VERY HIGH ENERGY γ-RAY EMISSION CONSTRAINTS FOR PSR B1951+32 FROM STACEE OBSERVATIONS

J. Zweerink[1], J. Kildea[2,7], J. Ball[1,8], J. E. Carson[1], C. E. Covault[3], D. D. Driscoll[3,9], P. Fortin[4], D. M. Gingrich[5,10], D. S. Hanna[2], A. Jarvis[1,11], T. Lindner[2,12], C. Mueller[2], R. Mukherjee[4], R. A. Ong[1], K. Ragan[2], and D. A. Williams[6]
[1] Department of Physics and Astronomy, University of California, Los Angeles, CA 90095, USA; zweerink@astro.ucla.edu
[2] Department of Physics, McGill University, Montreal, QC H3A 2T8, USA
[3] Department of Physics, Case Western Reserve University, Cleveland, OH 44106, USA
[4] Department of Physics and Astronomy, Barnard College, Columbia University, New York, NY 10027, USA
[5] Centre for Particle Physics, Department of Physics, University of Alberta, Edmonton, AB T6G 2G7, USA
[6] Santa Cruz Institute for Particle Physics, University of California, Santa Cruz, CA 95064, USA
Received 2008 June 17; accepted 2008 November 19; published 2009 March 5

ABSTRACT

The Solar Tower Atmospheric Cherenkov Effect Experiment (STACEE) is a ground-based telescope that uses the wave-front-sampling technique to detect very high energy (VHE) gamma rays. STACEE's sensitivity in the energy range near 100 GeV permits useful observations of pulsars with the potential to discriminate between various proposed mechanisms for pulsed gamma-ray emission. Based on the 11.3 hr of data taken during the 2005 and 2006 observing seasons, we derive an upper limit on the pulsed gamma-ray emission from PSR B1951+32 of $< 6.53 \times 10^{-11}$ photons cm^{-2} s^{-1} above an energy threshold of 117 GeV.

Key words: gamma rays: observations – pulsars: individual (PSR B1951+32)

Online-only material: color figures

1. INTRODUCTION

Pulsars were discovered in 1967 using a radio telescope at the Cambridge University (Hewish et al. 1968). Subsequent investigations identified pulsars with neutron stars and revealed that the pulsed emission arises as the emission region of the rotating neutron star periodically points toward the Earth. The number of known pulsars detected at radio wavelengths exceeds 1500 with around 70 of these seen in X-rays (Manchester et al. 2005; Kaspi et al. 2006). Additionally, the EGRET instrument on board the *Compton Gamma-Ray Observatory* strongly detected six pulsars emitting photons above 100 MeV (Crab, Geminga, Vela, PSR B1951+32, PSR 1706-44, and PSR 1055-32) (Nolan et al. 1996) and found a marginal signal from three additional pulsars—PSR B0656+14 (Ramanamurthy et al. 1996), PSR B1046-58 (Kaspi et al. 2000), and PSR J0218+4232 (Kuiper et al. 2000).

However, more than 40 years of research has not determined the mechanism(s) producing the pulsed radio through gamma-ray emission. In particular, three different general classes of models have been offered to explain how pulsars generate X-rays and gamma rays. All three models trace back to early standard magnetospheric models of neutron stars (Goldreich & Julian 1969). In these models, as the neutron star rotates, its intense magnetic field causes large electrical potentials that pull charged particles away from the surface of the star. Except for a few locations, these particles distribute themselves in such a way so as to short out the large electric fields. Those locations where the fields do not short out accelerate the charged particles that subsequently produce curvature and synchrotron radiation as they follow the magnetic field lines. The charged particles also scatter lower energy photons to produce high-energy gamma rays via the inverse-Compton process.

The three most popular models argue for different locations where the electric fields are produced. Consequently, they make different predictions regarding the temporal and energy distributions of the high-energy gamma rays. In the polar-cap model (Daugherty & Harding 1982, 1996), electrons are accelerated near the last closed field line right above the magnetic poles. As the electrons curve along the strong magnetic field lines they emit curvature radiation and scatter lower energy photons via the inverse-Compton process (Sturner & Dermer 1994). These photons interact with the magnetic field to produce e^+e^- pairs and more photons, eventually generating a shower of particles and photons. Scattered photons with sufficient energy produce enough e^+e^- pairs to short out the acceleration potential, resulting in a "superexponential" cut off of the energy spectrum between 1 and 20 GeV (Baring & Harding 2001).

Outer-gap (Cheng & Ruderman 1986; Romani 1996) models put the acceleration regions in the outer magnetosphere near the light cylinder. Charges pulled from the polar cap cannot populate the region between the null surface and the light cylinder resulting in a vacuum gap that causes particle acceleration. The magnetic field is weaker in this "outer gap," compared to near the polar cap so pair production does not limit the acceleration potential. Particle acceleration can also occur in a thin slot gap (that follows the last closed magnetic field line) connecting the polar-cap and outer-gap acceleration regions. Like the outer-gap models, the magnetic field in these slot-gap models (Arons 1983; Muslimov & Harding 2004) does not limit the acceleration potential. Thus, the outer-gap and slot-gap

[7] Present address: Fred Lawrence Whipple Observatory, Amado, AZ 85645, USA.
[8] Present address: GEMINI Observatory, Hilo, HI 96720, USA.
[9] Present address: Kent State University, Ashtabula Campus, Ashtabula, OH 44004, USA.
[10] also TRIUMF, Vancouver, BC V6T 2A3, Canada.
[11] Present address: Disney Interactive Media Group, North Hollywood, CA 91601, USA.
[12] Present address: Department of Physics and Astronomy, University of British Columbia, Vancouver, BC V6T 1Z1, Canada.

models can potentially produce photons of a few hundred GeV. Any detection of photons above 100 GeV would clearly favor the outer-gap and slot-gap models over the polar-cap model. Additionally, detailed measurements of the peak profiles of gamma rays above 10 MeV could discriminate between the various models.

Like most pulsars, PSR B1951+32 was first detected at radio wavelengths. Observations revealed an object in the CTB 80 radio synchrotron nebula with a 39.5 ms period (Kulkarni et al. 1988). Further observations and analysis demonstrated that the pulsar had a characteristic age of 1.1×10^5 yr, a surface magnetic field of 4.9×10^{11} G, and a rotational energy loss rate of 3.7×10^{36} erg s^{-1}. While both radio and X-ray observations show a single peak in the pulsar light curve (Kulkarni et al. 1988; Ögelman & Buccheri 1987), gamma rays detected by EGRET exhibit a double-peaked profile with neither peak matching the radio peak. No evidence for inter-peak emission is found in the EGRET data. Additionally, the EGRET data show no evidence for a cutoff in the pulsed emission up to $\sim$ 20 GeV (Ramanamurthy et al. 1995).

Previous observations at TeV energies have produced only upper limits on both steady and pulsed emission from PSR B1951+32 (Srinivasan et al. 1997). Recently, the MAGIC collaboration carried out observations above 75 GeV and found no evidence for pulsed emission (Albert et al. 2007). They quote a 95% C.L. upper limit onthe pulsed gamma-ray flux of $< 4.3 \times 10^{-11}$ photons cm^{-2} s^{-1} above 75 GeV.

2. OBSERVATIONS WITH STACEE

Located at the National Solar Thermal Test Facility (NSTTF) in Albuquerque, New Mexico, STACEE detects gamma rays above $\sim$ 100 GeV by sampling the Cherenkov light from air showers produced when a gamma ray interacts in the upper atmosphere. STACEE utilizes the large mirror area of a solar heliostat array to increase the sensitivity to low energy showers (E$\sim$100GeV) as compared with single-dish gamma-ray telescopes. Heliostats with 37 m^2 reflection area (25 1.2 m $\times$ 1.2 m mirrors comprise each heliostat) reflect the Cherenkov light to secondary mirrors on the receiver tower. The secondary mirrors then focus the light from each heliostat onto separate photomultiplier tubes (PMTs). STACEE uses 64 different heliostats to sample the Cherenkov shower front at 64 independent locations spread over a $\sim 2 \times 10^4$ m^2 area on the ground. The large mirror area allows STACEE to operate with an energy threshold around 100 GeV.

STACEE employs a two-level trigger system to identify air showers amidst the night-sky background light and to discriminate gamma rays from the far more abundant charged cosmic rays. The electronic signals from each PMT are AC-coupled, amplified and fanned-out for processing. In the trigger electronics chain, each PMT output is discriminated and digitally delayed in order to align the signals from each heliostat in a given subgroup. The delays correct for differences in light travel times from the heliostats to PMTs and in signal propagation times through the electronics. A minimum number of PMT channels are required to have fired within a given coincidence window of typically 12 ns. Normal STACEE operations use eight subgroups, each with eight PMT signals, and a Level-1 trigger requires five PMTs above threshold in a subgroup to fire. These Level-1 signals are aligned in time using additional delays. A full-detector (Level-2) trigger is generated upon exceeding a specified number of synchronous Level-1 triggers. Normal STACEE operations require five Level-1 triggers to generate a Level-2 trigger. Upon generation of a Level-2 trigger, a GPS-timestamped event is written to disk. Sky monitoring and heliostat status data are continuously recorded throughout an observing night by an independent system. For a more complete description of the STACEE detector and its operation, see Hanna et al. (2002) and Gingrich et al. (2005).

The PMT signals are also sent to high-speed flash analog-to-digital converters (FADCs) that are read out upon receipt of a Level-2 trigger. The information gained from sampling the PMT signals at 1GS s^{-1} using the FADCs is utilized in the offline data analysis to enhance STACEE's sensitivity to gamma rays.

STACEE's latitude of 34.°96N coupled with PSR B1951+32's declination of 32.°88 made for favorable observations. During three periods—2005 June–July, 2005 September, and 2006 June—a total of 10.0 livetime hours (11.3 hr of exposure) of PSR B1951+32 data were taken on clear, moonless nights at an average elevation of 82.5 deg. Usually, STACEE observes in ON/OFF mode where the source is tracked for 28 min (ON run) along with a background region (OFF run) following the same path on the sky. In order to maximize the amount of data recorded from PSR B1951+32, no background (OFF) observations were taken. Background observations were unnecessary because we searched for a signal in the phase plot after folding the trigger times at the radio pulsar period.

3. ANALYSIS

3.1. Cleaning and Gamma-ray Enhancement Analysis

STACEE observed PSR B1951+32 on 18 different nights during 2005–2006. After all the data for a given night were acquired, the trigger and FADC data were merged on an event-by-event basis, and the sky monitoring and heliostat status data were integrated into the subsequent file. Various data quality selection routines were applied on the fully merged data files. Sections of data, taken with malfunctioning hardware, unstable atmospheric conditions or excessive light contamination, were flagged and removed from the data analysis stream. For a detailed description of the standard cleaning procedure see Bramel et al. (2005).

Because the STACEE PSR B1951+32 data were obtained using nonstandard procedures, the application of data quality cuts also differed from the standard procedure. For example, the standard method for determining both the stability of sky conditions and changes in background light contamination relies on comparing the subgroup (Level-1) trigger rates between the ON and OFF runs. Under stable conditions, the rates and fluctuations of the subgroup triggers behave similarly for ON and OFF runs. For PSR B1951+32, no OFF runs were taken and thus a different stability check was adopted.

The Level-1 trigger rates for each run were binned in 10 s intervals and fit as a function of time. A quadratic polynomial was fit to the trigger rate as a function of elevation. If the residual between the fit and the recorded rate in any interval was more than 3 times the rms of all the residuals for that subgroup, the subgroup was flagged for that interval. Any time-interval with three flagged subgroups was declared bad and the 1 minute time period centered on the bin was removed from the analysis stream. Thus data taken under unstable weather conditions or with increased light contamination were eliminated. Additionally, all data taken with more than two sustained heliostat malfunctions were eliminated, as were any data without all 64 channels of FADC information. Data quality selection cuts eliminated 2.6 hr of observations resulting in

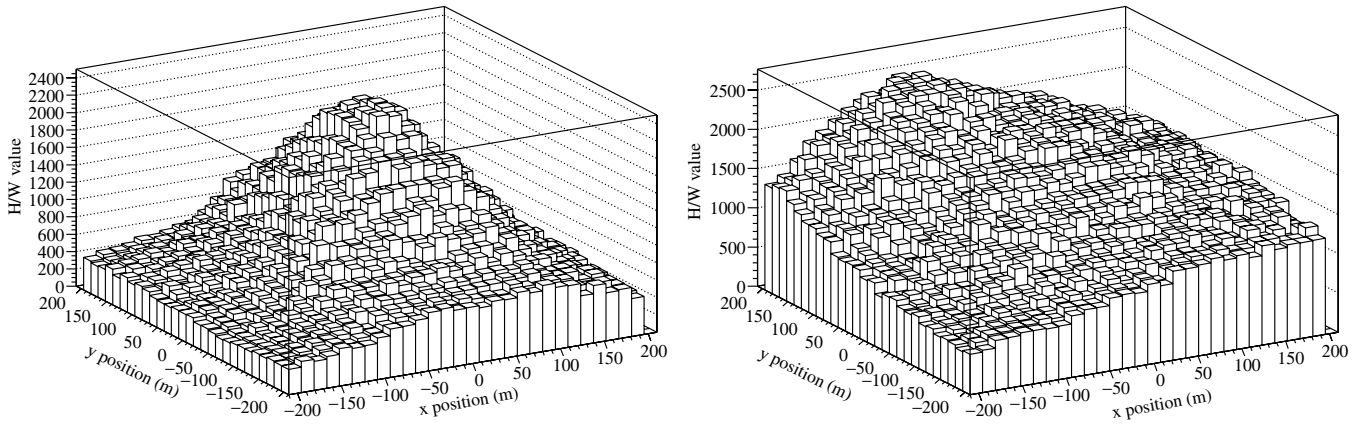

Figure 1. Grid alignment technique (as described in the text) applied to a simulated gamma-ray shower (left) and a simulated cosmic-ray shower (right). For each specified core location on the ground, the FADC data recorded by all STACEE channels are corrected for time delays and summed. The height-to-width ratio of the resulting pulse is calculated and plotted as a function of core location. The more uniform development of gamma-ray showers compared to cosmic-ray showers gives a peaked distribution.

7.4 hr of clean data to analyze for a pulsed gamma-ray signal.

Further cuts were applied to the STACEE data to discriminate between potential gamma rays and the background cosmic rays. In STACEE's energy range, gamma-ray shower fronts assume a spherical shape because most of the light originates from a small region where the number of particles in the shower is a maximum. In contrast, the hadronic nature of cosmic-ray interactions produces more variation in the shower development so cosmic-ray shower fronts are less uniform than those for gamma rays. A procedure referred to here as the *grid alignment technique* (Smith et al. 2006) exploits this difference to enrich the gamma-ray signal strength. Briefly, light-travel and detector transit time differences result in the FADC samples arriving at different times in their respective buffers. The light-travel differences rely on the position of the shower core relative to the heliostat layout. For each of a grid of assumed shower core locations, the FADC buffers are time-corrected, added together and the ratio of the resulting pulse height to pulse width is calculated. The assumed core location that gives the maximum height-to-width ratio is taken to be the true shower core. As shown in Figure 1, the distribution of this ratio drops off more quickly for gamma rays than for cosmic rays as a function of distance on the ground. Comparing the maximum ratio to the ratio at a given distance from the core provides a means to reject background cosmic rays. See Lindner et al. (2007) for a more complete description of the technique. Accounting for all data quality cuts and background rejection cuts, STACEE's energy threshold (defined as the peak of STACEE's response curve for a source with a Crab-like gamma-ray energy spectrum) is 117 GeV.

3.2. Timing Analysis

The arrival time of each candidate gamma-ray event recorded by STACEE is time stamped using a GPS clock. In order to properly compare the STACEE data with the pulsar's ephemeris, the arrival times for data passing all quality and background rejection cuts were transformed to the solar system barycenter using the JPL DE200 Planetary and Lunar Ephemeris (Standish 1982, 1990).

To check our timing procedures we used a special setup of three PMTs to record optical data from the Crab pulsar. The location of two peaks at the proper phase after barycentering, seen in Figure 2, verified the optical path of the STACEE detector and the proper functioning of the barycentering code.

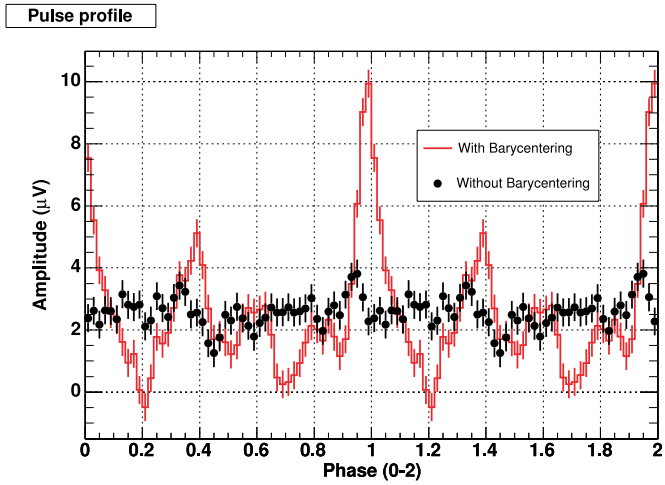

Figure 2. Phaseogram for optical data from the Crab pulsar recorded by STACEE using a special setup (Fortin 2005). The pronounced peaks at the proper phase after converting the arrival times from the local time to solar system barycenter time confirm the proper functioning of STACEE's UTC timing and the barycentering code.

(A color version of this figure is available in the online journal.)

Table 1
Ephemeris of PSR B1951+32 (provided by A. Lyne 2008, private communication)

Position Epoch	2450228.4144 JD
Right Ascension	$19^h52^m58\overset{s}{.}2756912$
Declination	$32°52'40\overset{''}{.}6823860$
Pulsar Epoch	2453727.31329982 JD
ν	25.29522592356(47) Hz
$\dot{\nu}$	$-3.72866(47) \times 10^{-12}$ Hz s^{-1}
$\ddot{\nu}$	$-1.67(16) \times 10^{-22}$ Hz s^{-2}

Table 1 shows the ephemeris for PSR B1951+32 that was used to convert from local to solar system barycentered times. Figure 3 shows the barycenter arrival time of each candidate gamma-ray event recorded by STACEE (and that passed all cuts) folded at PSR B1951+32's period. The shaded regions correspond to the location of the primary and secondary peaks detected by EGRET (Ramanamurthy et al. 1995). No evidence for pulsed gamma-ray emission was found. Using the method

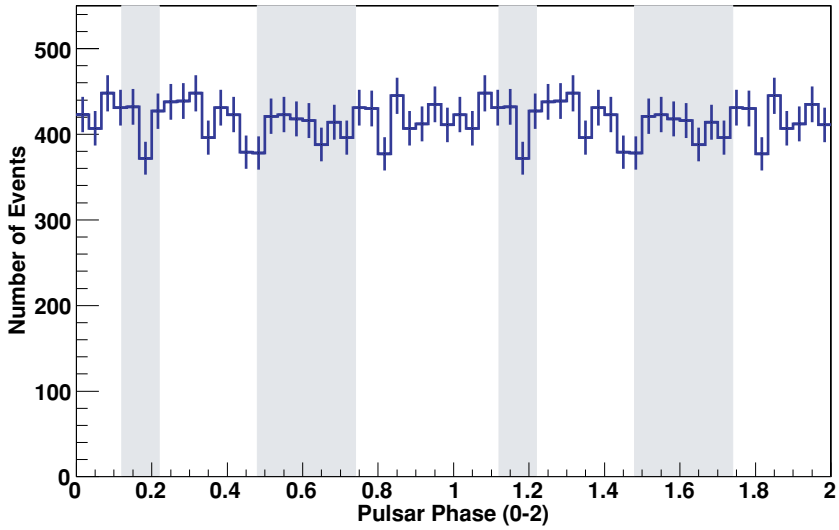

Figure 3. Phaseogram of candidate STACEE gamma-ray events from PSR B1951+32 folded using the radio pulsar's ephemeris. The shaded regions correspond to the location of the primary peak (0.12–0.22) and the secondary peak (0.48–0.74) as seen by EGRET (Ramanamurthy et al. 1995). No evidence for a signal is seen.
(A color version of this figure is available in the online journal.)

of Helene (1983), a 99.9% C.I. upper limit on the number of pulsed gamma-ray events in the STACEE data was calculated.

The effective area for STACEE was determined by propagating a set of gamma-ray shower simulations through a computer model of STACEE's optics and electronics. The energy spectrum of the simulated gamma-ray showers matched the spectrum measured for PSR B1951+32 by EGRET (Nolan et al. 1996) and their impact parameters were distributed uniformly over STACEE's collection area. The effective area and energy threshold were calculated by comparing the number of simulated showers with the number that triggered the computer model. The effective area was used to convert the limit on the number of gamma-ray events in the STACEE data into a limit on the pulsed gamma-ray emission from PSR B1951+32. The resulting integral flux upper limit is $< 6.53 \times 10^{-11}$ photons cm^{-2} s^{-1} above an energy threshold of 117 GeV.

4. DISCUSSION

The mechanisms at work in pulsars that produce the X-ray and gamma-ray emission remain poorly understood. Consequently, any observational constraints help refine theoretical models. Based on measurements below 20 GeV by EGRET, PSR B1951+32 is one of the most promising candidates to produce gamma rays with energies detectable by current ground-based instruments. The STACEE shower-front sampling gamma-ray detector was used to observe this pulsar during 2005 and 2006. Analysis of 7.4 hr of cleaned data revealed no pulsed gamma-ray emission resulting in a integral flux upper limit of $< 6.53 \times 10^{-11}$ photons cm^{-2} s^{-1} above 117 GeV.

Given this energy threshold, a detection of pulsed emission by STACEE would clearly have favored the outer-gap model. The magnetic fields required for emission in polar-cap models strongly attenuate gamma-ray emission above a few tens of GeV. However, the latest polar-cap (Harding 2001) and outer-gap (Hirotani 2007) models predict sharp cutoffs in pulsed gamma-ray emission from PSR B1951+32 below 60 GeV. Thus, this new upper limit does not provide any discrimination between the two models. Other gamma-ray experiments (such as MAGIC (Albert et al. 2007)) have provided more constraining upper limits at lower energy thresholds than those presented here. Nevertheless, this work represents the first constraints on the VHE gamma-ray emission from PSR B1951+32 using the shower-front sampling technique.

STACEE was decommissioned in the summer of 2007, and so no further data will be taken by STACEE to improve upon this limit. However, other more sensitive gamma-ray telescopes have recently begun observations. In the northern hemisphere, VERITAS (Holder et al. 2008) and MAGIC (Ferenc et al. 2005) have energy thresholds below 100 GeV for PSR B1951+32 (H.E.S.S.'s location in the southern hemisphere (Hinton 2004) means its energy threshold for this object is higher). NASA recently launched the Fermi Gamma-ray Space Telescope (Ritz 2007) that can detect gamma rays with energies up to 300 GeV. The overlapping energy range of these instruments provides the first opportunity to measure the gamma-ray emission from PSR B9151+32 (and gamma-ray pulsars in general) with no gaps in the energy spectrum. Thus, observations over the next few years will definitively map out the emission properties of PSR B1951+32.

We are grateful to the staff of the National Solar Thermal Test Facility who have made this work possible and to Andrew Lyne for providing the ephemeris for PSR B1951+32. This work was funded in part by the U.S. National Science Foundation, the Natural Sciences and Engineering Research Council of Canada, Fonds Quebecois de la Recherche sur la Nature et les Technologies, the Research Corporation, and the University of California at Los Angeles.

REFERENCES

Albert, J., et al. 2007, ApJ, 669, 1143
Arons, J. 1983, ApJ, 266, 215
Baring, M. G., & Harding, A. K. 2001, ApJ, 547, 929
Bramel, D. A., et al. 2005, ApJ, 629, 108
Cheng, K. S., & Ruderman, M. A. 1986, ApJ, 300, 500
Ferenc, D., et al. 2005, Nucl. Instrum. Methods Phys. Res. A, 553, 274
Fortin, P. 2005, PhD thesis, McGill University
Daugherty, J. K., & Harding, A. K. 1982, ApJ, 252, 337
Daugherty, J. K., & Harding, A. K. 1996, ApJ, 458, 278
Gingrich, D. M., et al. 2005, IEEE Trans. Nucl. Sci., 52, 2977
Goldreich, P., & Julian, W. H. 1969, ApJ, 157, 869

Hanna, D. S., et al. 2002, Nucl. Instrum. Methods Phys. Res. A, 491, 126
Harding, A. K. 2001, in AIP Conf. Proc., 599, X-ray Astronomy: Stellar Endpoints, AGN, and the Diffuse X-ray Background, ed. N. E. White, G. Malaguti, & G. G. C. Palumbo (Melville, NY: AIP), 150
Helene, O. 1983, Nucl. Instrum. Methods Phys. Res., 212, 319
Hewish, A., et al. 1968, Nature, 217, 709
Hinton, J. 2004, New Astron. Rev., 48, 331
Hirotani, K. 2007, ApJ, 662, 1173
Holder, J., et al. 2008, in AIP Conf. Proc., 1085, High Energy Gamma-ray Astronomy: Proceedings of the 4th International Meeting on High Energy Gamma-ray Astronomy (Melville, NY: AIP), 657
Kaspi, V. M., Roberts, M. S. E., & Harding, A. K. 2006, in Compact Stellar X-ray Sources, ed. W. Lewin & M. van der Klis (Cambridge: Cambridge Univ. Press), 279
Kaspi, V. M., et al. 2000, ApJ, 528, 445
Kuiper, L., et al. 2000, A&A, 359, 615
Kulkarni, S. R., et al. 1988, Nature, 331, 50
Lindner, T., et al. 2007, Astropart. Phys., 28, 338
Manchester, R. N., Hobbs, G. B., Teoh, A., & Hobbs, M. 2005, AJ, 129, 1993; see http://www.atnf.csiro.au/research/pulsar/psrcat/
Muslimov, A. G., & Harding, A. K. 2004, ApJ, 606, 1143
Nolan, P. L., et al. 1996, A&AS, 120, 61
Ögelman, H., & Buccheri, R. 1987, A&A, 186, L17
Ramanamurthy, P. V., et al. 1995, ApJ, 447, L109
Ramanamurthy, P. V., et al. 1996, ApJ, 458, 755
Ritz, S. 2007, AIPC, 921, 3
Romani, R. W. 1996, ApJ, 470, 469
Smith, D. A., et al. 2006, A&A, 459, 453
Srinivasan, R., et al. 1997, ApJ, 489, 170
Standish, E. M. 1982, A&A, 114, 297
Standish, E. M. 1990, A&A, 233, 252
Sturner, S. J., & Dermer, C. D. 1994, in AIP Conf. Proc., 304, The Second Compton Symposium, ed. N. Geherls, J. P. Norris, & C. P. Fichtel (College Park, MD: AIP), 106